POLITECNICO
MILANO 1863

DIPARTIMENTO DI MECCANICA

mecc

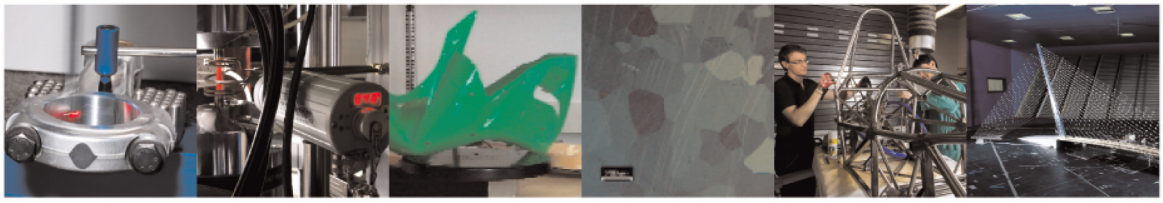

On the efficiency of machine learning for fatigue assessment of post-processed additively manufactured AlSi10Mg

E. Maleki;S. Bagherifard;S. M. J. Razavi;M. Bandini;A. du Plessis;F. Berto;M. Guagliano

This is a post-peer-review, pre-copyedit version of an article published in International Journal of Fatigue. The final authenticated version is available online at:
https://doi.org/10.1016/j.ijfatigue.2022.106841

© <2022>

This content is provided under CC BY-NC-ND 4.0 license

DIPARTIMENTO DI MECCANICA ■ POLITECNICO DI MILANO
via G. La Masa, 1 ■ 20156 Milano ■ EMAIL (PEC): pecmecc@cert.polimi.it
http://www.mecc.polimi.it
Rev. 0

On the efficiency of machine learning for fatigue assessment of post-processed additively manufactured AlSi10Mg

E. Maleki[a], S. Bagherifard[a*], S.M.J. Razavi[b], M. Bandini[c], A. du Plessis[d,e], F. Berto[c], M. Guagliano[a]

[a] Department of Mechanical Engineering, Politecnico di Milano, Milano, Italy
[b] Peen Service srl, Bologna, Italy
[c] Department of Mechanical and Industrial Engineering, Norwegian University of Science and Technology (NTNU), Trondheim, Norway
[d] Research Group 3D Innovation, Stellenbosch University, Stellenbosch, South Africa
[e] Faculty of Engineering, Nelson Mandela University, Port Elizabeth, South Africa

*Corresponding author, Email: sara.bagherifard@polimi.it

Abstract

Laser powder bed fusion (LPBF) is receiving widespread attention for its capability to build components with complex geometries. Post-processing can address the adverse effects of various imperfections exhibited in LPBF parts in their as-built state, including inhomogeneous microstructure, tensile residual stresses and poor surface quality. In a recent experimental study, we investigated the influences of different post-processing techniques of heat treatment and shot peening as well as their combination on rotating bending fatigue behavior of V-notched LPBF AlSi10Mg samples. Herein, we further examined those samples regarding the specific parameters that directly influence fatigue performance with the aim to develop a deep learning based approach by means of artificial neural network. The effect of yield stress, ultimate tensile strength, elongation, porosity, microhardness, compressive residual stresses, and surface roughness and morphology were assessed and implemented in the model. Fatigue behavior of the samples was predicted and analyzed using sensitivity and parametric analyses. The obtained results reveal the high potential of deeply learned neural network for unlocking the role of post-processing on the fatigue performance of LPBF AlSi10Mg specimens.

Keywords: laser powder bed fusion, notch, shot peening, fatigue, heat treatment

1. Introduction

Laser powder bed fusion (LPBF) process is among the most promising additive manufacturing (AM) processes in terms of fabricating fine features and complex geometries in an economical fashion [1–3]. Due to layer-wised nature of LPBF process and the corresponding intricate physical phenomena (inducing thermal gradient and very fast cooling rate of melt pool about 10^6 K/s) [4,5], the fabricated materials are commonly characterized by various internal and surface defects [6]. Metallic LPBF materials commonly have anisotropic microstructure [7], multiple internal defects such as trapped voids, lack of fusion and key hole defects [8,9], residual stresses [10,11], and low surface quality [12]. These internal and surface imperfections have negative impact on the mechanical performance of the LPBF materials [13,14]. The low surface quality of these materials in the as-built state can be specified by rough surfaces with extremely irregular morphologies [15]; surface defects include unmelted and partially melted feed-stock, stairwise features and spatters and balling effects [12,16–18]. The surface imperfections are affected by feed-stock (powder) material specifications, design and geometry of the part, the considered LPBF process parameters and fabrication strategy [19]. The randomly positioned surface defects act as local stress concentration zones causing early crack initiation [20,21], which will directly impact the mechanical performance of the materials under quasi-static and fatigue loading [22,23]. Therefore, applying surface post-treatments such as shot peening can play a crucial role in modulating the effect of the surface related issues [24].

To capture the link between the mentioned factors and their effect on the mechanical response of AM components, powerful tools such as machine learning (ML)-based systems can be used. ML-based systems such as neural networks (NNs) have gained considerable attention recently, due to their efficiency in comprehensive modelling of different complex phenomena in various fields of science and engineering [25,26]. Generally, a NN has three main input, hidden and output layers [27]. Preliminary generation in artificial NN namely shallow neural network (SNN) has one or two hidden layers. These networks are mostly trained by back-propagation (BP) algorithm [28,29]. Mostly experimental data set is utilized for constructing a NN. The large data sets needed to develop SNN can be quite

limiting by considering the high cost of experiments [30]. Taking advantage of deep learning approaches such as deep belief network (DBN) and restricted Boltzmann machine (RBM) introduced by Hinton *et al.* [31,32], it is now conceivable to construct deep neural network (DNN) via greedy layer-wised models with pre-training by a small experimental data set. Stacked auto-encoder (SAE) as a pre-training technique in DNN was presented for developing DNN with a smaller data set offering a very high accuracy for the predicted results [33–36]. Different types of NNs have been used in the field of AM [37]. The studies which have used NN in AM and their outputs, the considered AM technology and feed-stock material are reported in Table 1.

Table 1. List of the studies applying NN based methods in the field of AM

NN type	AM process	Used material	Output parameter	Ref.
SNN	PBF[1]	Al	Bead width	[38]
	DED[2]	P420	Cladding width	[39]
	PBF	AISI 316L	Porosity	[40]
	DED	Cu coated steel	Bead width Bead height	[41]
	DED	Ti	Porosity	[42]
	PBF	AISI 316L	Fatigue life	[43]
	PBF	AISI 316L Ti-6Al-4V AlSi10Mg	Fatigue life	[44]
DNN	DED	AISI 316L	Thermal history	[45]
	PBF	Ti-6Al-4V AlSi10Mg Inconel 718 AISI 316L 17-4 PH	Surface quality	[46]
	PBF	AISI 316	Classification of melt-pool	[47]
	PBF	Ti-6Al-4V	Tensile strength Ultimate strength Elongation	[48]

[1] PBF: Powder bed fusion
[2] DED: Direct energy depositions

Regarding the modelling of fatigue behavior of AM materials via NN, Zhan *et al.* [43,44] firstly used continuum damage mechanics theory for fatigue life estimation and then the numerically computed fatigue lives were fed to the network for prediction. In their study, experimental data set was not used but they comprehensively assessed the performance of developed NN with 2 hidden layers by different statistical criteria with a maximum accuracy of 0.9.

Herein, following our previous study [49], which investigated the influence of various post-treatments of heat treatment (HT), shot peening (SP) and their combination as a hybrid treatment on fatigue strength of V-notched LPBF AlSi10Mg samples, a computer-aided AI based method was utilized for fatigue life prediction and analysis. To the best of the authors' knowledge, for the first time, a deep learning based approach was used for modelling the fatigue response of as-built and post-treated LPBF material via NN using experimental results to feed the system. Different parameters of yield stress, ultimate tensile strength, elongation, relative density, surface hardness, depth of hardness, surface residual stresses, maximum value and the depth of residual stresses field, surface roughness, surface modification factor and stress amplitude were gathered as inputs and fatigue life was regarded as the output of the developed network. NN modelling was performed by constructing different types of networks including SNN, DNN and stacked auto-encoder assigned deep neural networks (SADNN) for prediction and further analyzing of the fatigue performance of the treated V-notched LPBF AlSi10Mg specimens. The results obtained from different models were then compared and the one with the highest efficiency was selected for further analyses as an optimum network.

2. Experimental procedure

Following our previous study [49], LPBF AlSi10Mg samples with the same thermal and surface post-treatments were considered for further experimental analysis. Fig. 1a and 1b reveal the relevant scanning strategy and dimensions of the V-shaped notched specimens, respectively. Two types of post-treatments namely T6 thermal treatment (HT) and two different SP treatments (SP1 and SP2) were applied via steel and ceramic shots [49]. Table 2 lists the details of the used SP processes per-

formed on as-built and heat treated specimens. SP is a cold working treatment which bombards the surface of the part with high energy impacting media under a controlled level of intensity and coverage [50]. SP can effectively increase the surface layer hardness by applying surface layer grain refinement and it can also induce high compressive residual stresses (CRS) from surface through the interior of the bulk material. The schematic representation of the SP process and the affected properties including roughness, hardness and CRS are depicted in Fig. 1c. Fig. 1d for instance, compares the V-notched LPBF AlSi10Mg samples before and after applying SP with ceramic shots.

Table 2. SP process parameters applied on LPBF AlSi10Mg specimens [49]

SP	Shot type	Shot hardness (HRC)	Shot standard	Shot diameter (mm)	Almen intensity (A 0.001 inch)	Surface coverage (%)
SP1	Steel	50	S 170	0.43	10	100
SP2	Ceramic	62	Z 100	0.15	5	100

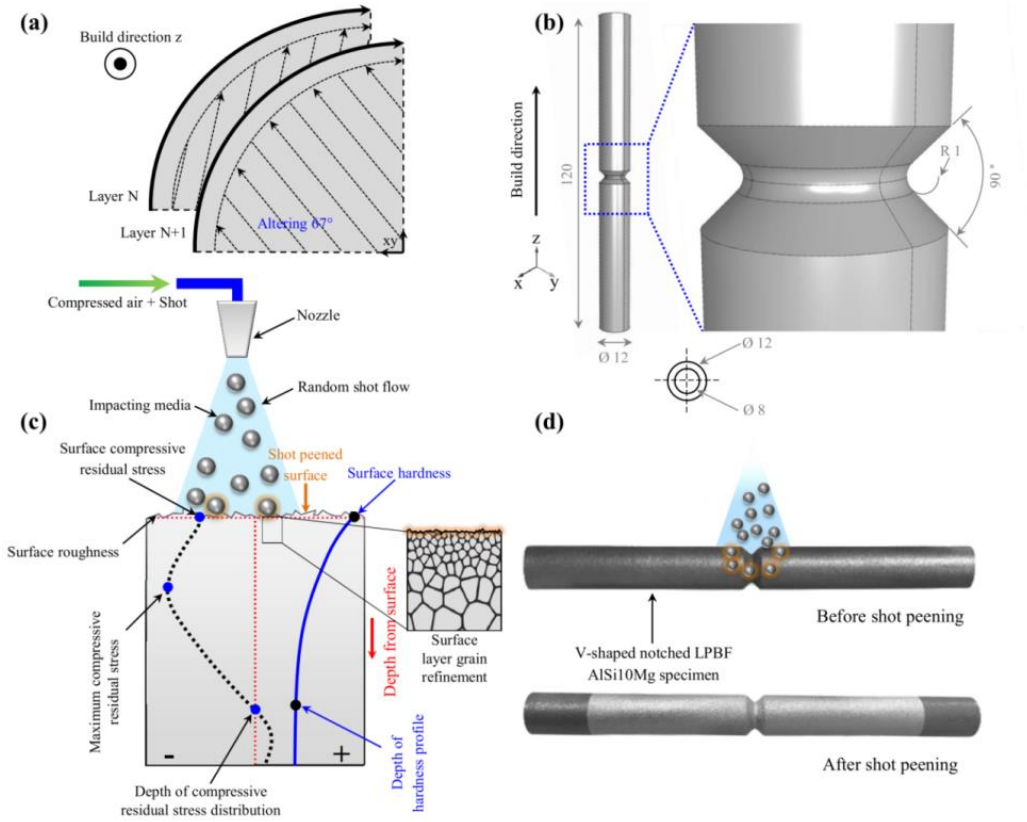

Fig. 1. (a) The used scanning strategy in each fabricated layer (b) Geometry of the V-notched LPBF specimen considering the vertical build direction (c) Schematic illustration of SP treatment and affected properties of the target material (d) Schematic representation of V-notched LPBF AlSi10Mg samples before and after applying SP with ceramic shots.

Considering the as-built (AB) sample and the applied post-treatments, six sets of samples including AB, AB+SP1, AB+SP2, AB+HT, AB+HT+SP1 and AB+HT+SP2 were considered to study the influences of sole and hybrid post-treatments.

Relevant experimental procedures for observations of surface morphology, microhardness and residual stress measurements, micro-CT porosity analysis as well as rotating bending fatigue tests were already presented in our previous study [49]. Different stress amplitudes of 10-140 MPa with run-out limit of 3×10^6 cycles were considered for performing fatigue tests. Additional experiments carried out in this study include Micro-CT analysis to assess the surface texture and morphology of the samples and fracture site analysis was also performed considering the failed samples state before and after fatigue tests. Cross-sectional optical microscopy (OM) of fractures site was performed using Nikon Eclipse LV150NL optical microscope. In addition, surface roughness of the notch root was

evaluated by Mahr Perthometer (PCMESS 7024357) equipped with MFW 250 probe with a tip diameter of 5 μm. EN ISO 4287 standard [51] was followed for sampling and cut-off wavelengths and the filtering parameters. Three samples and three paths were used for each set of samples on the random surface areas for roughness measurements. Roughness parameter of arithmetic mean (R_a) was obtained for each set.

3. Deep learning process

NNs consist of computational nodes (neurons) which can extract the existing relationship between the various variables inspired from the human's brain. NNs have been also employed for fatigue behavior modelling of shot peened conventional materials [29,52,53] but not for analyzing the response of LPBF material to shot peening. Schematic illustration of a single layer network developed by *r* and *s* numbers of input parameters of *p* and output parameters of *a*, respectively, with the assigned weight matrixes *w*, bias vectors *b*, linear combiner *u* and transfer function *f*, is depicted in Fig. 2a.

Different types of networks were implimented with trial and error approach in order to achieve desirable network structure and parameters with the highest performance. From 89 samples in the data set, 80% of the data set (71 samples) was regarded for training and the remained 20% (18 samples) was considered for testing of the developed networks. A random function was used to select data for training and testing steps. The data used for training was not employed in the testing step. Accuracy of the predicted results of NNs was assessed by correlation coefficient (R^2) for examination of networks performance. This coefficient is determined as [54]:

$$R^2 = \frac{\sum_{i=1}^{n}\left(f_{EXP,i} - F_{EXP}\right)\left(f_{ANN,i} - F_{ANN}\right)}{\sqrt{\sum_{i=1}^{n}\left(\left(f_{EXP,i} - F_{EXP}\right)^2\left(f_{ANN,i} - F_{ANN}\right)^2\right)}} \quad (1)$$

in which, *n* is the number of considered data to the network, and f_{EXP} and f_{ANN} represent the experimental and predicted values, respectively. In addition, F_{EXP} and F_{ANN} can be calculated as follows:

$$F_{EXP} = \frac{1}{n}\sum_{i=1}^{n} f_{EXP,i} \quad (2.a)$$

$$F_{ANN} = \frac{1}{n}\sum_{i=1}^{n} f_{ANN,i} \quad (2.b)$$

In this study, the optimum LPBF process parameters obtained in Bagherifard *et al.* [55] were used to modulate the sample properties in terms of reduced porosity and enhanced strength and surface quality. However, the obtained experimental results may not be totally generalizable and sub-optimal fabrication parameters could affect the initial mechanical properties and fatigue behavior of the LPBF samples. Therefore, since the modelling approach relies on experimental data obtained for a specific combination of process parameters, any variations in fabrication parameters could affect the accuracy of the predicted results.

The methodology used in this study, which is based on the accuracy of the predicted results, is presented in Fig. 2b. Fig. 3a indicates the considered inputs and output in this study. Twelve different parameters of yield strength, ultimate strength, elongation, relative density, surface hardness, depth of hardness, surface CRS, maximum in-depth value of CRS, the depth of CRS field, surface roughness, surface modification factor and stress amplitude were considered as inputs and fatigue life was regarded as the output of the developed NNs.

Fig. 3b and 3c present the schematic illustrations of an ordinary SNN constructed using two hidden layers as well as the architecture of a DDN with four hidden layers and the assigned SAE, respectively. BP method was considered for developing all networks. The number of neurons in each layer is one of the main parameters of the network structure, which should be considered carefully in the development of the networks. Generally, networks performance can be enhanced by increasing the number of neurons, although it may increase the computational costs as well [53]. A DDN can be assumed as a modified SNN with more hidden layers. Based on the number of samples in the data set

used to feed the network and also the nature and complexity of the considered phenomena, DNNs can be constructed with pre-training step [56]. As shown in Fig. 3c, SAE is assigned in between the layers of DNN for pre-training of the fed data. In the development of a fully inter-connected SADNN with *y* layers, *y-1* SAEs are needed [34]. In the developed SADNN with six layers including input layer, 4 hidden layers, and output layer, five SAEs were used. In this study, the number of used neurons in every SAE is equal to the one used in the corresponding DNN layer. Therefore, with respect to the number of layers and neurons, in the six layers SADNN with 12+(24+12+9+6)+1 architecture and SAEs with 12+(24)+12, 24+(12)+24, 12+(9)+12, 9+(6)+9, 6+(3)+6 structures were assigned. After feeding the data to DNN, the SAE catches the inputs as its own input and output data. Then, the data were processed and the outputs of the first hidden layer were transmissed to the next SAE as the new input. This process keeps going up to reaching to the last SAE. After pre-training of data with all SAEs, the achieved initial values of weight and bias in each layer $w^y(0)$ were assigned to the corresponding layer in the DNN to start modelling with a progressed SADNN.

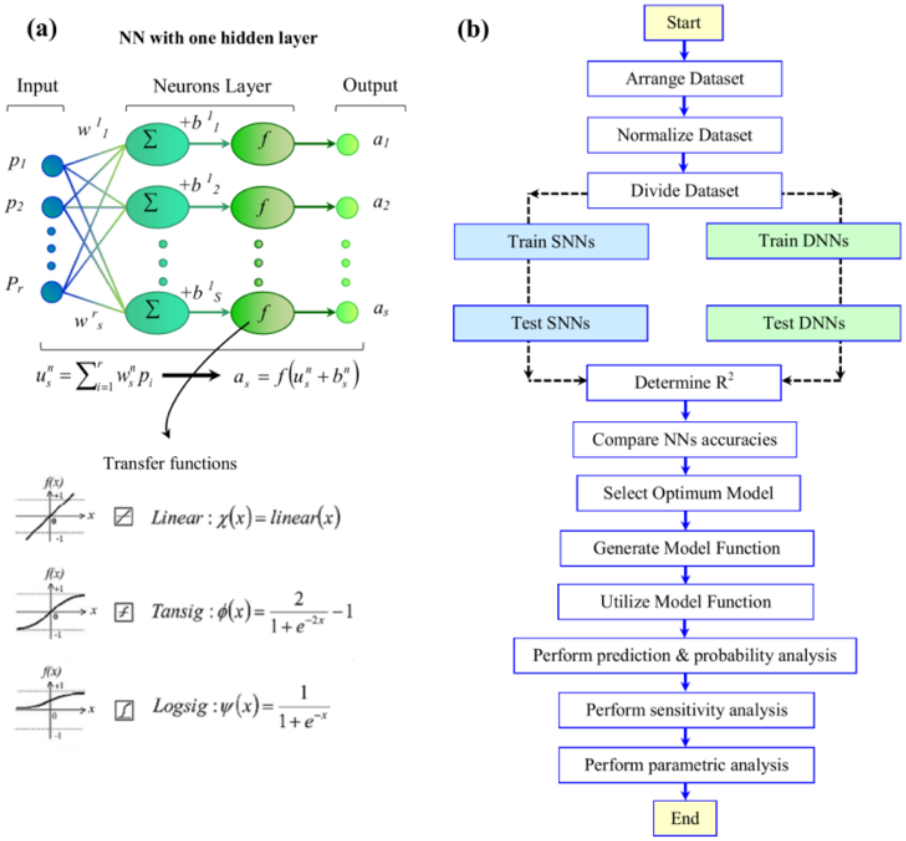

Figure 2. (a) Architecture of single layer network with one hidden layer with respect to the weight matrixes (*w)*, bias vectors (*b)*, linear combiner (*u)* and different types of transfer functions (*f) of Linear, Tansig and Logsig* (b) The used methodology considering R^2 value (accuracy) for networks developing.

After examination of the different NNs for obtaining the optimum structures of NNs with the highest accuracy and best performance, the corresponding model function of the selected network that consists of the values of weights and biases was generated for further sensitivity and parametric analyses. The model function of considered SADNN with six layers can be generated as follows:

$$a^1 = f^1(w^1 i + b^1) \quad (3.a)$$

$$a^2 = f^2(w^2 i^1 + b^2) \quad (3.b)$$

$$a^3 = f^3(w^3 i^2 + b^3) \quad (3.c)$$

$$a^4 = f^4(w^4 i^3 + b^4) \quad (3.d)$$

$$a^5 = f^5(w^5 i^4 + b^5) \quad (3.f)$$

$$a^6 = M(m(1)) = f^6(w^6 i^5 + b^6) = f^6(w^6 f^5(w^5 f^4(w^4 f^3(w^3 f^2(w^2 f^1(w^1 i + b^1) + b^2) + b^3) + b^4) + b^5) + b^6) \quad (4)$$

where a^1, a^2, a^3, a^4 and a^5 are the output parametersof the 1st to 5th layers, respectively. Also, M function corresponds the considered 12 inputs to the fatigue life $m(1)$ as an output. In addition, sensitivity analysis was performed using the achieved weight matrix of network using Garson's equation, which can be determined as [57]:

$$I_j = \frac{\sum_{m=1}^{N_h}\left(\left(\frac{|W_{jm}^{ih}|}{\sum_{k=1}^{N_i}|W_{km}^{ih}|}\right)\times|W_{mn}^{ho}|\right)}{\sum_{k=1}^{N_i}\left\{\sum_{m=1}^{N_h}\left(\frac{|W_{km}^{ih}|}{\sum_{k=1}^{N_i}|W_{km}^{ih}|}\right)\times|W_{mn}^{ho}|\right\}} \quad (5)$$

where I_j is the relative importance of the j^{th} input related to the output. While the numbers of input and hidden neurons are defined as N_i and N_h , respectively, and W is the connection weight. The superscripts i, h, and o in the equation refer to input, hidden and output neurons.

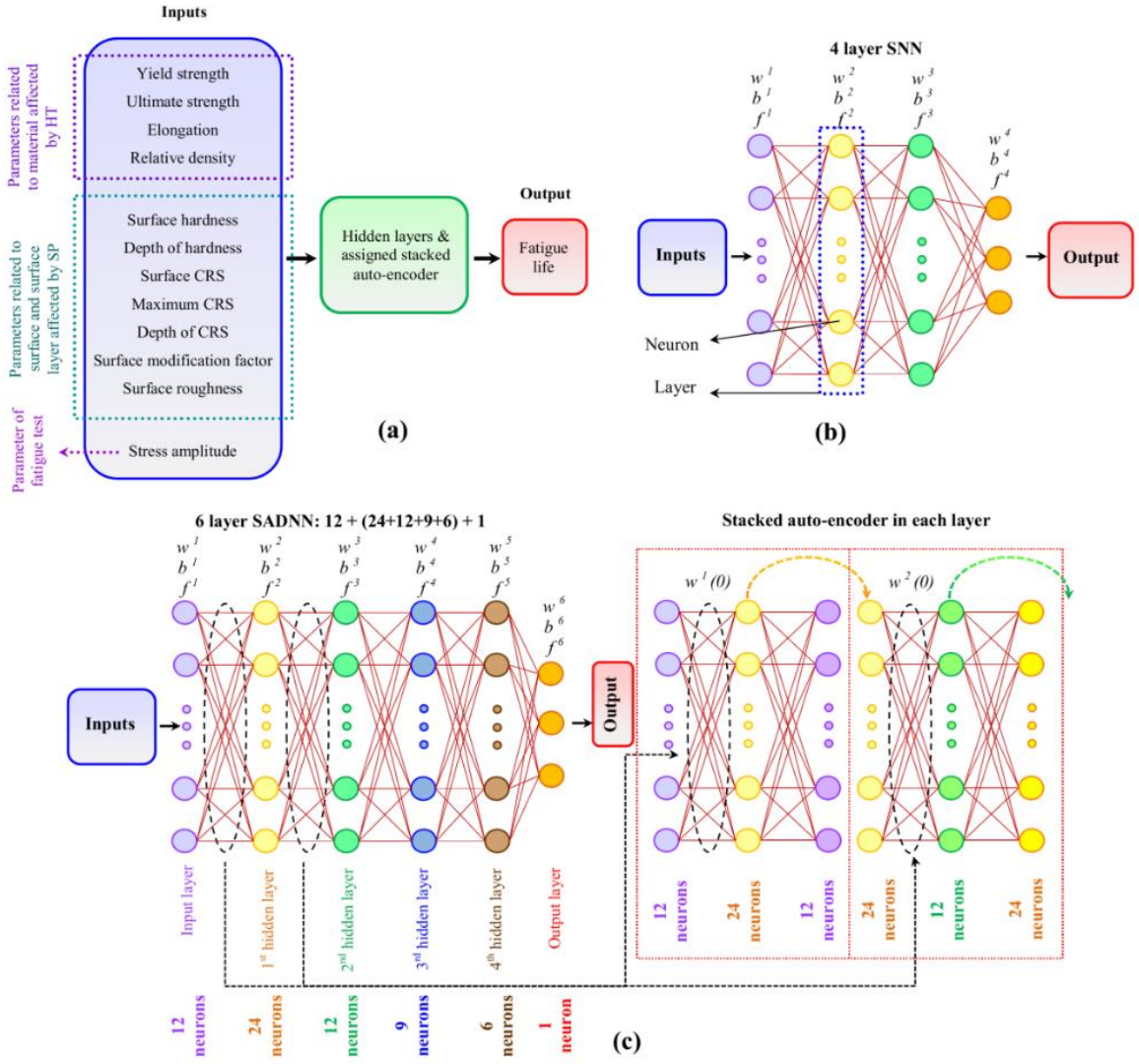

Fig. 3. (a) The considered inputs and output in this study. Inputs of yield and ultimate strengths, elongation, relative density, surface hardness, depth of hardness, surface CRS, maximum value of CRS, depth of CRS field, surface roughness, surface modification factor and stress amplitude were fed to the NNs to model the output parameter of fatigue life. Schematic illustrations of (b) 4 layers SNN and (c) 6 layers DNN with the assigned SAEs.

4. Results and discussions

4.1. Experimental results

4.1.1. Porosity analysis

Detailed evaluations of the porosities in all sets of samples were performed by color imaging of the size and locations of pores in 3D using micro-CT analysis, as represnted in Fig. 4a [49]. Fig. 4b exhibits the cross-sectional images for detailed micro-CT assessment of porosity distribution by color coding for all sets of samples. The porosity analysis as a function of height in the color coded images indicates the lowest porosity around the notch root. Average porosities (in %) of 0.47, 0.52, 0.44, 0.39, 0.42 and 0.43 were obtained in the notch area for AB, AB+SP1, AB+SP2, AB+HT, AB+HT+SP1 and AB+HT+SP2, respectively.

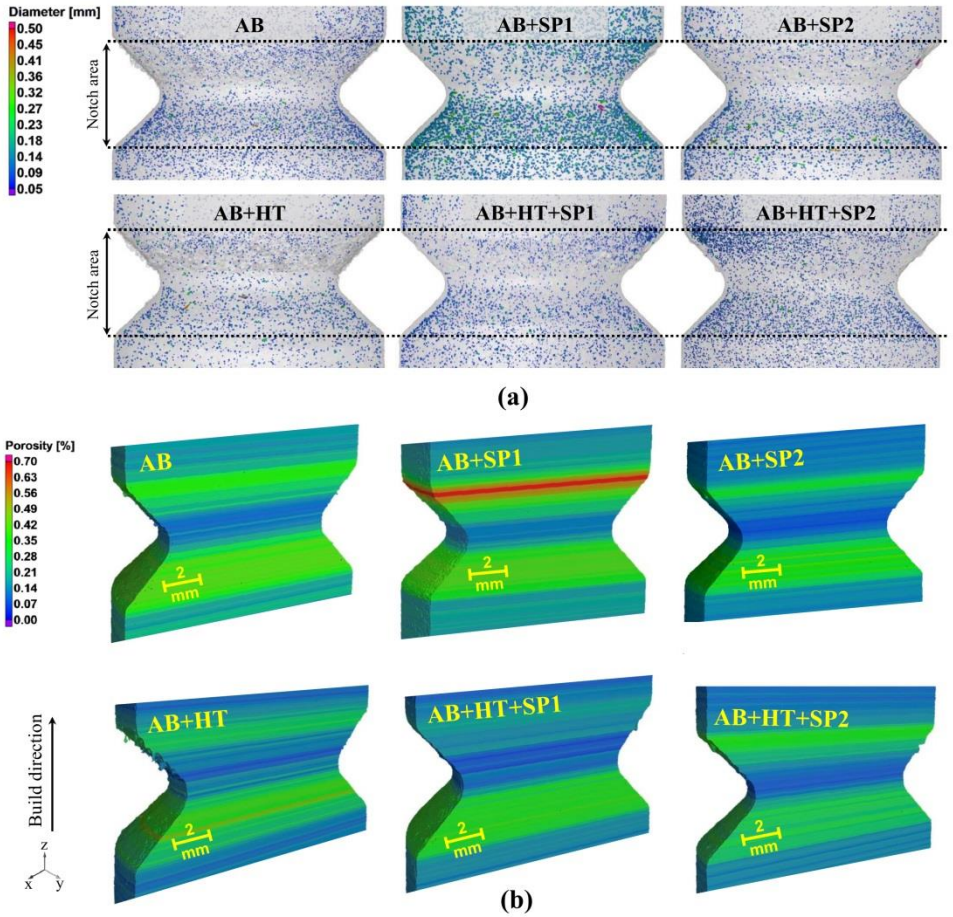

Fig. 4. Micro-CT analysis of (a) 3D porosity D for all series of samples using color coding [49] and (b) cross-sectional images of detailed porosity assessment by color coding as a function of height with respect to the notch root.

4.1.3. Surface morphology and roughness

Surface textures of the samples obtained by micro-CT scans in the notch area as well as the smooth areas above and below the notch area are presented in Fig. 5a. Considering AB sample and the relevant deviation of the surface roughness, it can be seen the cylindrical areas have the lowermost roughness in comparison with notch area. In the notch area, three different regions of upward surface, notch root area and downward surface can be observed with distinct surfacetextures. Downward and

upward surfaces show very low surface quality, in particular on the downward faces, due to complex thermal history and lower cooling rate as well the presence of inclined surfaces and overhang [58]. Quantitative comparison reveals the highest surface roughness for the downward surface with a high density of surface defects, followed by the upward surface and ultimately the notch root, respectively. Similar trend with comparable roughness values can be seen on the AB+HT samples as HT has no effect on surface roughness and morphology. Besides, the surface imperfections including unmelted and partially melted powders, balling defects and spatters , are mostly removed in the shot peened samples in all regions of notch area.

The results of surface roughness measurements in the notch root in terms of R_a indicate that, although the surface defects and irregularity are notably moderated after applying SP in both AB and AB+HT states, the surface roughness is slightly enhanced (lower than 0.6 µm) after SP. This is mainly caused by the formation of dimples after the impacts of shots and the corresponding surface plastic deformation. This roughness increase was more notable for SP2 as it implemented harder shots, despite using a lower Almen intensity compared to SP1. Based on the results of roughness measurements on the notch root, the values of 4.34, 4.52, 4.83, 4.30, 4.56 and 4.87 µm were found for AB, AB+SP1, AB+SP2, AB+HT, AB+HT+SP1 and AB+HT+SP2 samples, respectively, in terms of R_a.

Fig. 5b presents the scanning electron microscopy (SEM) micrographs of surface morphologies in the notch root area of all sets of samples; these observations indicate that the surface defects were considerably removed after SP [49]. The results indicated that in the shot peened samples, AB+SP2 and AB+HT+SP2 samples have more uniform surfaces compared to the ones treated with steel shots (AB+SP1 and AB+HT+SP1) and therefore SP2 is more effective in modifying the surface morphology of the notch root. In this study, besides considering surface roughness in terms of R_a parameter, a new surface modification factor is presented as an index of effectiveness of the SP treatment on homogenizing the surface quality of the notched LPBF samples. In implementation of NNs, normalization of data setbefore feeding to NNs must be carried out. Among the standard normalizing methods is dividing the values of each input parameter by the corresponding highest value in the data set. Therefore, whole data set used for developing the network will be in the range of 0-1 [59]. In order to define the surface modification factor, a numerical criterion in the intrerval of 0-1 (i.e. 0, 0.5 and 1), was considered to specify the improvement of the surface quality after applying different SP treatments of SP1 and SP2. As shown in Fig. 5c, considering the range from worst surface quality to the best surface quality in the notch area, numeric criteria of 0, 0.5 and 1 were assigned to (AB or AB+HT), (AB+SP1 or AB+HT+SP1) and (AB+SP2 or AB+HT+SP2) pairs, respectively.

4.1.4. Mechanical properties

Different mechanical properties including microhardness, residual stresses and fatigue response of the samples were investigated. The data for microhardness and residual stress measurements are adopted from our previous study [49]. Microhardness measurements were performed on the longitudinal cross section (*yz-plane*) of the samples along notch root direction to better analyze the local effects of SP treatments as depicted in Fig. 6a [49]. The AB+HT samples, due to their higher ductility and lower tensile strength, exhibited lower microhardness compared to the as-built state [55]. As expected, the surface layer of the SP treated samples exhibited increased microhardness. SP2 in comparison with SP1 was more efficient in surface layer hardening of the notch root as ceramic shots with lower shot diameter and higher hardness utilized in SP2, resulted in increasing the number of effective impacts on the notch root, despite their lower intensity.

Residual stress distributions from the exterior surface through the material interior were measured on the smooth area of all samples using XRD analysis as illustrated in Fig. 6b [49]. It can be observed that tensile residual stresses of AB samples were relaxed after heat treatment and a maximum CRS of -45 MPa was obtained for the AB+HT samples. Moreover, because of primary differences of shot-substrate properties, the results revealed that applied SP post-treatments were more efficient in inducing CRS on AB series compared to the AB+HT ones [55]. Between the two SP treatments, SP1, with higher kinetic energy, generated a deeper CRS distribution. The SP treatments were more effective in terms of the maximum CRS in AB series compared to the HT ones, due to the initial different hardnesses [55]. The results of the measurements on the cylindrical part of the samples

indicate that in both cases of as-built and heat treated states, SP1 with higher Almen intensity induced deeper CRS field (530 μm) compared to the samples treated with SP2 (480 μm). Surface CRS of −83 and -65 MPa were measured in AB+SP1 and AB+SP2 samples, respectively. Also, maximum in-depth CRS of −157 MPa at the depth of 180 μm and −170 MPa at the depth of 200 μm were introduced in the AB+SP1 and AB+SP2 samples, respectively. Similar trend was also observed in the heat treated samples and surface CRS of -46 and -31 MPa, increased to maximum in-depth CRS of -113 MPa at the depth of 400 μm and −103 MPa at the depth of 140 μm for AB+HT+SP1 and AB+HT+SP2 samples, respectively.

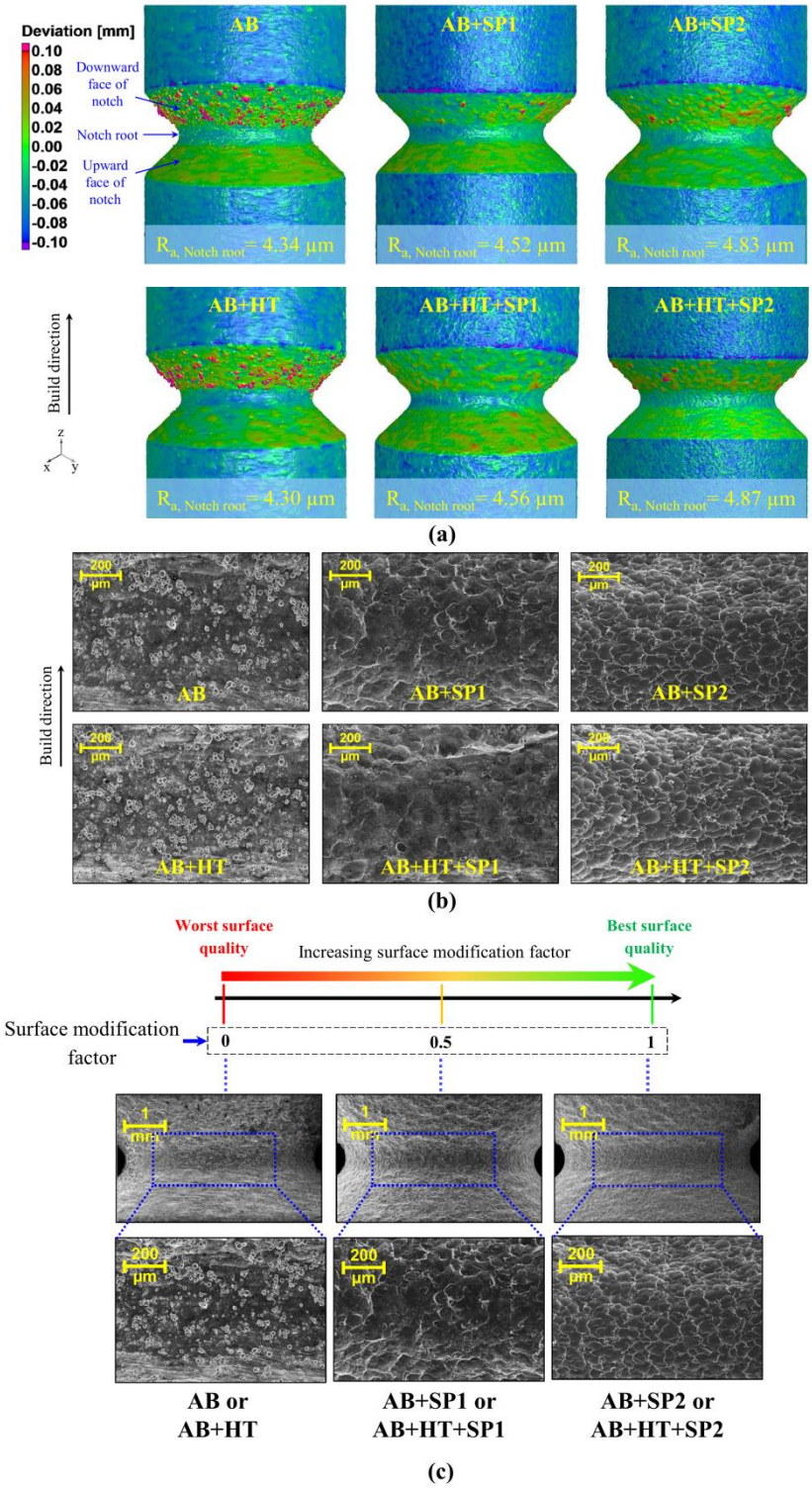

Fig. 5. (a) Surface morphology of samples obtained by micro-CT scans in the notch area as well as the smooth areas above and below the notch considering roughness deviation with respect to the notch root direction (b) SEM micrographs of surface morphologies in the notch root for all samples [49] (c) Surface modification factor defined to describe the notch root surface quality ranging from 0 for the worst to 1 for the best surface quality among the tested series.

The Fatigue life of all sets of notched LPBF AlSi10Mg samples at different loads considering a run out limit of 3×10^6 cycles was obtained as reported in Fig. 6c and 6d. The results indicate considerable fatigue life improvement after applying combined HT and SP treatment as a hybrid post-treatment.

Also, dealing with the sole effects of each post-treatment, SP exhibited more efficiency than HT in fatigue behavior improvement thanks to surface layer hardening, inducing high CRS and surface morphology modification. For instance, considering stress amplitude of 110 MPa the fatigue life of AB sample with 1.26×10^4 cycles increased up to 1.19×10^6 and 2.11×10^6 cycles in AB+SP1 and AB+SP2 samples, respectively. In the heat treated samples, the fatigue life of AB+HT sample with 2.47×10^4 cycles improved up to 2.01×10^6 and 2.95×10^6 cycles in AB+HT+SP1 and AB+HT+SP2 samples, respectively. Also, standard deviation of $\pm1.1\times10^3$, $\pm1.0\times10^5$, $\pm1.5\times10^5$, $\pm2.4\times10^3$, $\pm1.1\times10^5$, $\pm1.3\times10^5$ cycles were obtained for AB, AB+SP1, AB+SP2, AB+HT, AB+HT+SP1 and AB+HT+SP2 respectively. The XRD measurements for obtaining residual stresses were performed in the areas far from the notch zone, due to practical limitations regarding homogeneous material removal. The scatter observed in the fatigue life obtained per each series could be also correlated to the fact that the XRD measurements were not directly performed in the notch area. Considering the different thermal histories of the up skin, notch root and down skin zone, we could expect variations of the induced residual stresses in these areas that could not be introduced and thus are neglected in the measurements.

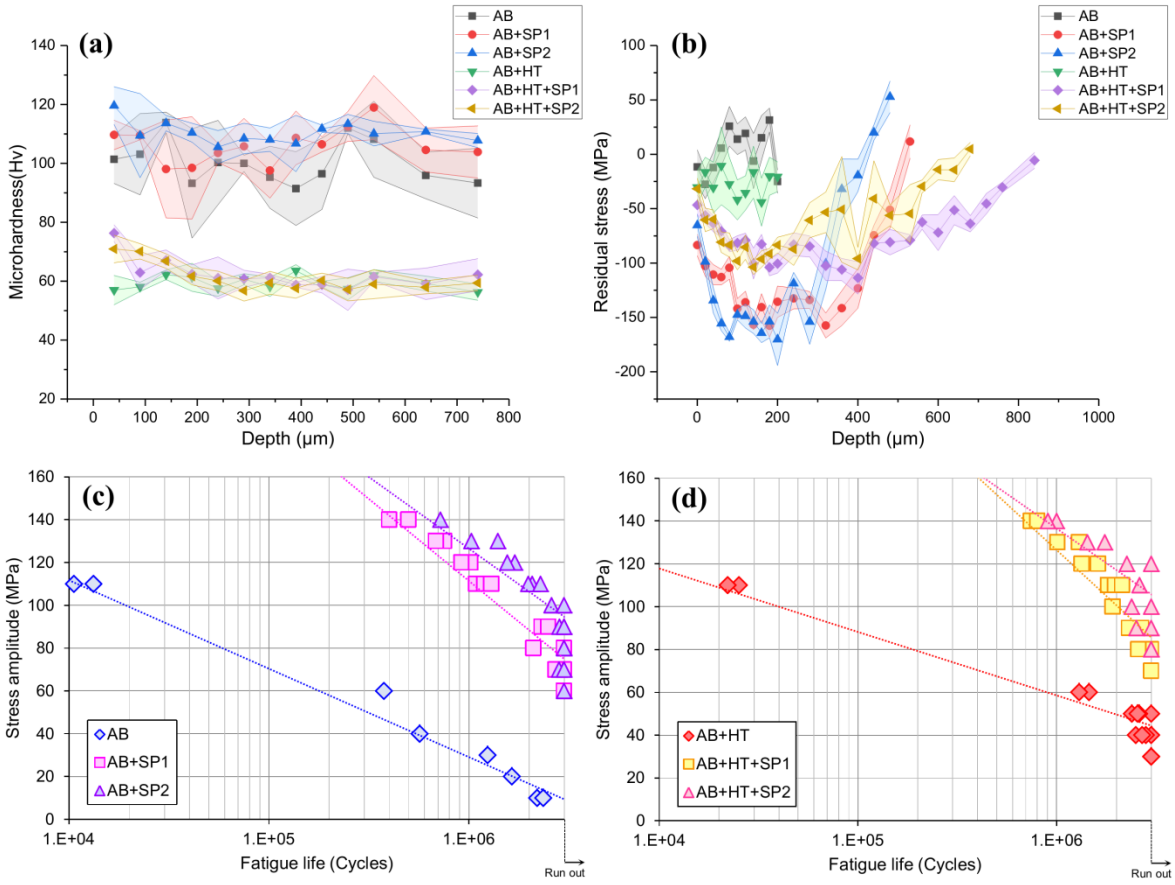

Fig. 6. (a) Microhardness profiles in the notch root and (b) residual stress distributions in all samples measured from the top surface through the material interior [49]. Rotating bending fatigue test data for (c) AB, AB+SP1 and AB+SP2, and (d) AB+HT, AB+HT+SP1 and AB+HT+SP2 V-notched LPBF AlSi10Mg samples.

Fractured samples were analyzed in the two main directions: the oneperpendicular and the one parallel to the fracture surface. Fig. 7a represents cross-sectional OM micrographs of the fracture surface of AB and AB+HT samples as well as their SEM top view fractographs. Detailes of the fracture surfaces of these samples focusing on crack initiation sites are presented in Fig. B (in Appendix B). In addition, SEM images of the different areas of fracture surfaces in all sets of samples are shown in our previous study [49].

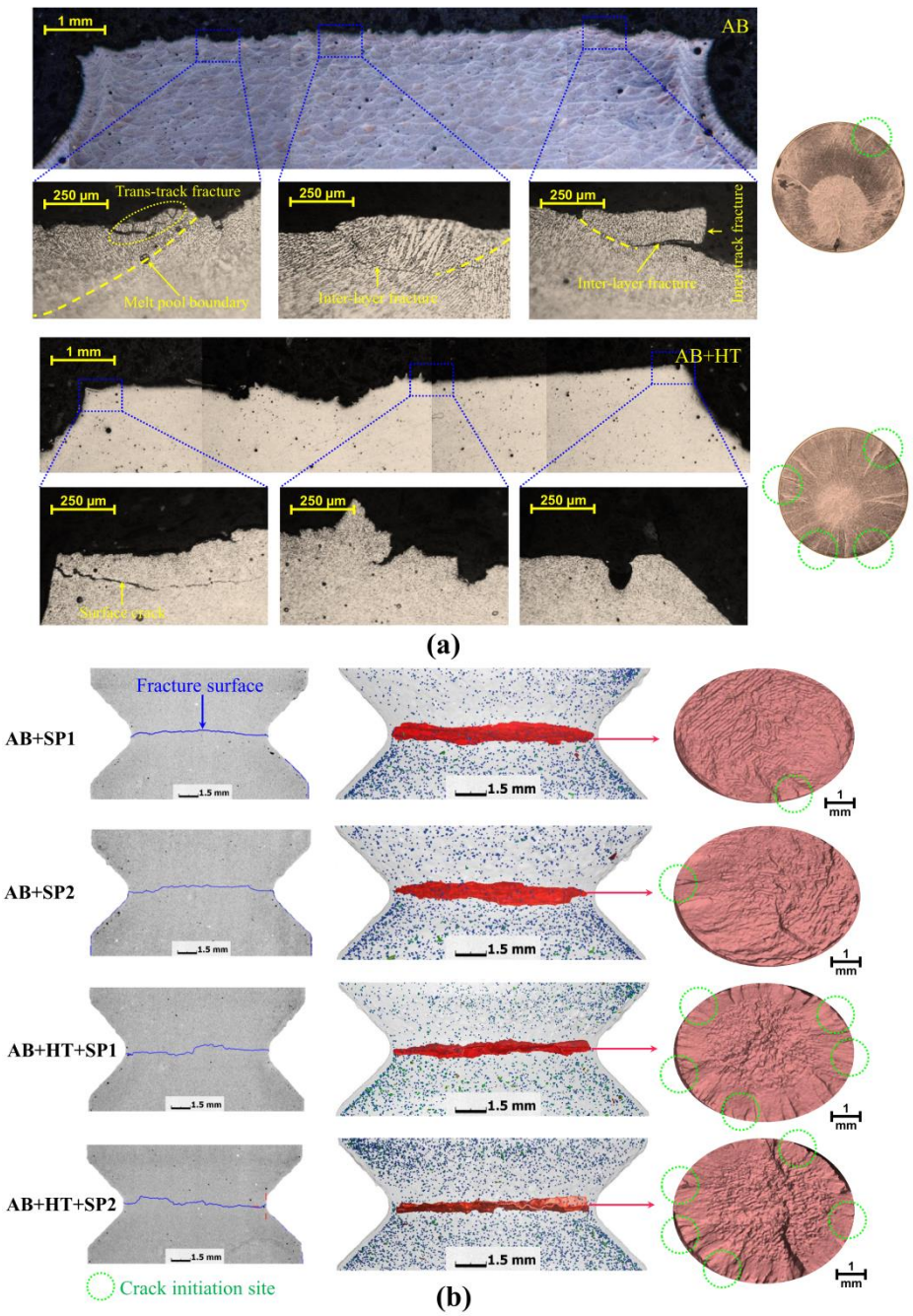

Fig. 7. (a) Cross-sectional OM observations of the fractured surface in AB and AB+HT samples and the SEM images of the top view of the fracture surface (b) Cross-sectional and top view micrographs of the fracture surfaces in the shot peened samples obtained by overlapping the micro-CT data before/after fatigue tests.

Fractography images indicate that the fatigue failure initiated from the surface in all cases and propagated through the bulk. In the AB sample, SEM image reveals that the dominant fatigue crack initiated from the surface irregularities in one side of the sample and propagated through the cross section along a relatively straight direction. In addition, in the magnified OM images, trans-track fracture, which implied crack propagation through the inner part of the melt pool, can be seen paired also with features indicating mixed inter-track and inter-layer fractures. These forms of fractures are described in detail in the study of Girelli *et al.* [60]. Dealing with AB+HT sample, on the other hand, no dominant crack was detected and multiple surface cracks contributed to the failure. Also, the cross-sectional view of the failed AB+HT sample reveals a rougher fracture plane in comparison with AB sample due to the presence of multiple crack propagation planes and their coalescence.

The fracture surfaces of the shot peened samples were investigated by overlapping micro-CT data before and after fatigue tests. The exact location of the fracture planes illustrating the local features can be seen in Fig. 7b. In AB+SP1 and AB+SP2 samples, the same patterns in terms of crack initiation site and fracture plane straightness compared to the AB sample can be observed. Also, similar trends were found for AB+HT+SP1 and AB+HT+SP2 samples in terms of multiple crack initiation sites and rough fracture plane in comparison with AB+HT sample. The laser track features are clearly visible on the fracture surfaces of the AB series, while they are faded in the HT ones that are dominantly characterized with higher deformation on the final fracture (central) area. It should be also mentioned that crack initiation mechanism of the LPBF materials was investigated in details in the study carried out by Qian *et al.* [61]. They used LPBF Ti-6Al-4V samples fabricated in different building orientations of 0, 45 and 90° with respect to a horizontal plane for analysing the fatigue bahavior. The results indicated that the fatigue cracks were initiated from defects of the LPBF material both at high-cycle and very high-cycle fatigue regime regardless the build orientations of the samples.

4.2. Modelling results

The experimental results as listed in Appendix A were used for developing the network. In order to consider the base material in both as-built and heat treated states, the corresponding yield and ultimate strengths and elongation were used, adopted from an study by Bagherifrad *et al.* [55] considering the approach implemented in [27,29,62].

Various types of NNs were constructed to compare the accuracy of the predicted results. 12 neurons were considered in the input layer and 1 neuron was utilized in the output layer in all the developed networks. Network parameters of 0.185 learning rate and Logarithmic-Sigmod (*logsig*) transfer function were employed.

After comparing all the constructed NNs, the one which had the highest efficiency in terms of R^2 (detailes of performance evaluation of networks were already mentioned in section 3) was selected for further analyses as an optimum network. The accuracies of the predicted results of fatigue life as the output of the modelling achieved from SNNs are shown in Fig. 8a considering the increased number of neurons in each layer. The results show that by increasing the neuron's number, the accuracy of the SNNs increase. In the developed SNNs, the network with 12+50+50+1 layers with the accuracy of 0.95 and 0.94 for training and testing steps, respectively, showed the best performance.

Accuracy comparison of the predicted fatigue lives obtained by different NNs are illustrated in Fig. 8b. It can be observed that SADNN with an architecure of 12+(24+12+9+6)+1 had the highest efficiency and showed accuracies of 0.991 and 0.983 for training and testing steps, respectively. In addition, the results reveal that using SAEs for pre-training in the developed DNNs can increase the accuracy of the results. For instance, in the DNN model with 3 hidden layers, the accuracy of the predicted results increased from 0.962 up to 0.974 after employing pre-trained data thanks to SAEs. The SADNN was selected for performing the sensitivity and parametric analyses. To validate the performance independency of the selected SADNN from the order of the data fed initially to the network, other three data set with different orders were considered for both training and testing steps. The performance examination of the chosen SADDN fed with other generated datasets is represnted in Table 3. In all the considered orders of data sets, minimum accuracies of 0.99 and 0.98 were obtained for training and testing steps, respectively.

The network model function needed to perform sensitivity and parametric analyses was constructed after the optimal network was selected using the methods shown in Fig. 2b. The V-notched LPBF AlSi10Mg samples' fatigue behavior was examined using sensitivity analysis to determine the impact of each considered input parameter. For the purpose of comparing the samples' fatigue life under various input conditions, a parametric analysis was also performed. Figures 8c and 8d show the results of the sensitivity analysis in terms of the relative relevance of each parameter and the corresponding rankings.

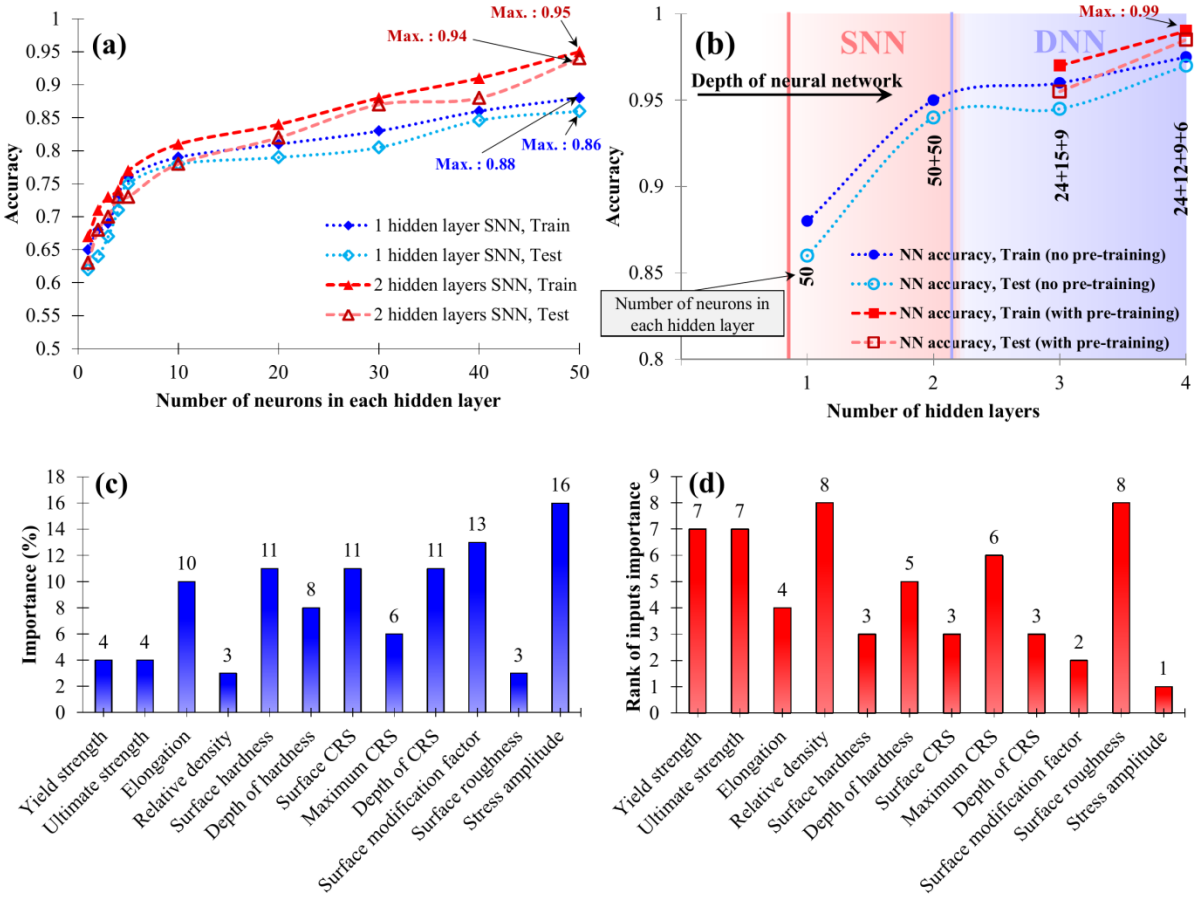

Fig. 8. (a) The effect of number of neurons per layer in SNNs with 1 and 2 hidden layers on the accuracy of the estimated fatigue life (b) The comparison of the accuracy of the estimated fatigue life obtained by SNNs, DNNs and SADNNs models; the results of sensitivity analysis in terms of (c) relative importance of each input and (d) the corresponding rank for fatigue life improvement in notched LPBF AlSi10Mg samples.

Table 3. The accuracy of the predicted fatigue lives in training and testing steps determined from the selected SADNN fed with three different data sets

Data set	R^2	
	Training	Testing
Initial data set	0.9913	0.9839
1st randomly selected data set	0.9907	0.9810
2nd randomly selected data set	0.9911	0.9836
3rd randomly selected data set	0.9901	0.9812

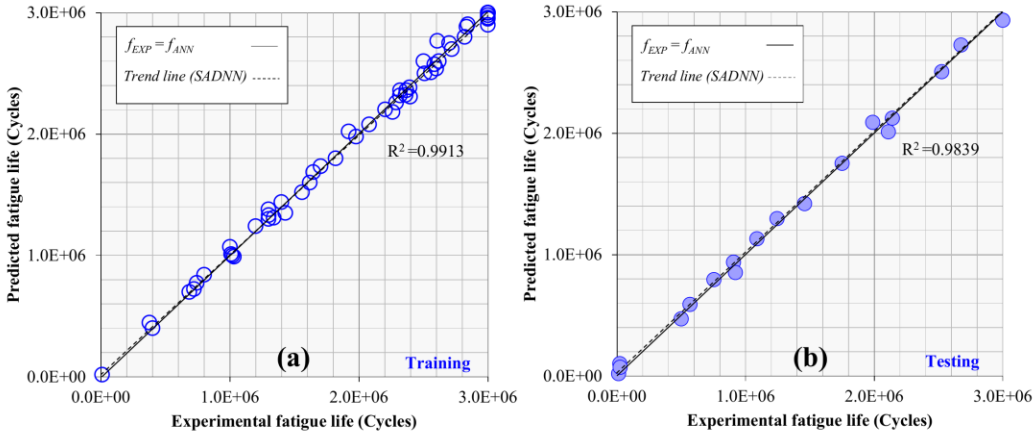

Fig. 9. The experimental and anticipated values of fatigue life in (a) training and (b) testing procedures.

The findings demonstrate that all of the input parameters analyzed and allocated to SADNN have a direct impact on fatigue behavior, albeit with varying degrees of relative significance. The first rank of the fatigue test was shown to be more sensitive to stress amplitude than the second rank, which is the most important parameter in the fatigue test. Similar outcome was also obtained in the fatigue response of the as-received and shot peened conventionally fabricated materials in [29]. Surface modification factor, which specifies the extent of surface morphology modification, was in the second rank. In the third rank, three parameters of surface hardness, surface CRS and depth of CRS with the same relative importance were placed. Elongation of the base material, which indicates material ductility, was at the fourth rank followed by the depth of hardness in the fifth rank. Accordingly, maximum CRS, yield and ultimate strengths and both relative density and surface hardness were following as ranks of 6, 7 and 8, respectively. Sensitivity analysis results indicated that among the parameters induced by SP, the increase of surface modification factor was the most effective; indeed, improved surface quality was found to fully mask the adverse effect of surface roughness. On the other hand, the parameters that can delay crack initiation and growth were found to be of little importance. Increased surface hardness and surface CRS is supposed to delay crack initiation whereas higher depths of CRS can play a significant role in delaying crack propagation and growth. Among the parameters affected by the heat treatment, elongation was found of higher importance compared to the yield and ultimate strengths.

Fig. 9 presents the comparative diagram of the fatigue lives estimated using the selected SADNN with the obtained experimental data. Fatigue life was estimated also using the generated model function obtained from the SADNN. S-N diagrams for all samples considering experimental and predicted values are presented separately in Fig. 10. Instead of relying on discrete data from the experiments, fatigue life was estimated continually. As a result, it is possible to calculate the associated fatigue life for various applied stress amplitudes. Results from the predictions are quite consistent with those obtained from the experiments. Furthermore, the likelihood of the expected results is explored when continuous intervals are taken into account. Also, the probability of the fatigue life was estimated by using kernel probability density estimation (KPDE) which is a non-parametric method to estimate the probability density of a scattered data set. For instance, probability density analyses of the experimental and predicted results for AB sample are shown in Fig. C (in Appendix C).

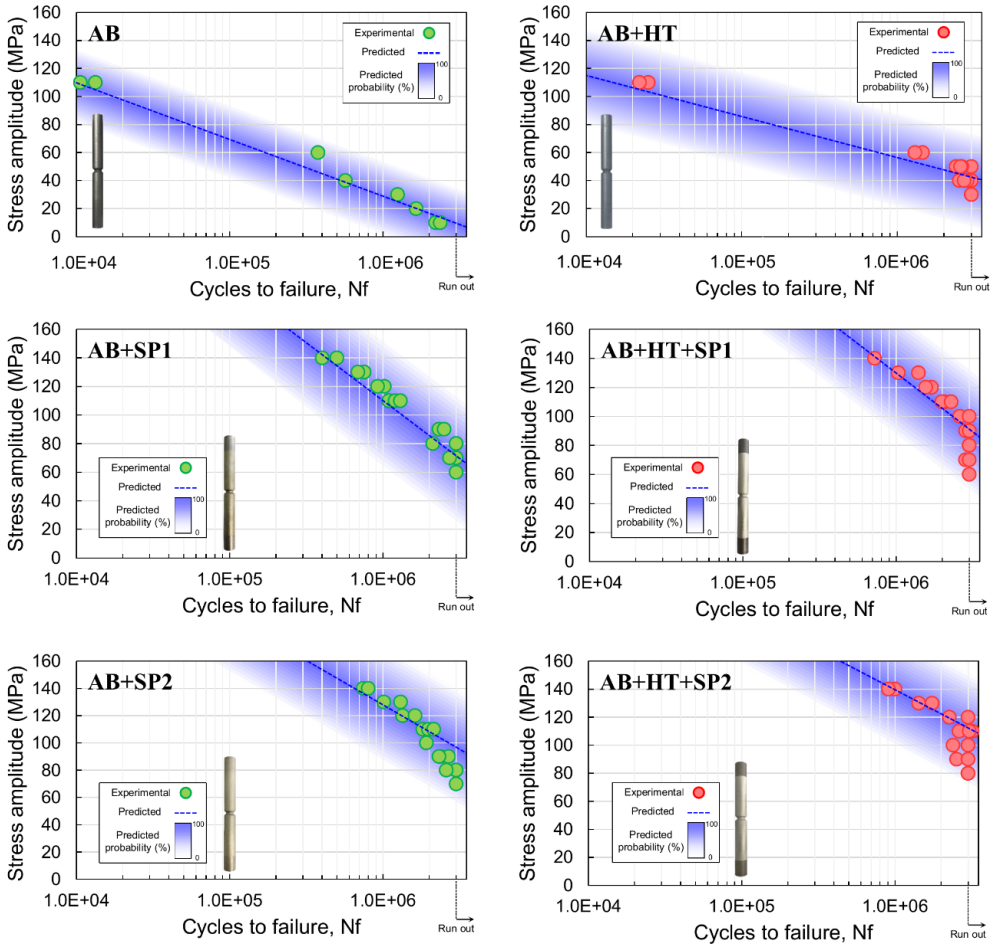

Fig. 10. S-N diagrams for fatigue life prediction of all notched LPBF AlSi10Mg samples considering the probability of the predicted results.

Parametric analysis on fatigue behavior of the notched AlSi10Mg LPBF samples was carried out considering the five important input parameters of stress amplitude, surface modification factor, surface hardness, surface CRS and depth of CRS according to the sensitivity analysis results. In the implementation of the parametric analysis, the whole range of experimental data was considered for all input parameters. The 2D contours of the results of parametric analysis depicted in Fig. 11, reveal significant effect of stress amplitude range. Qian and Lei [63] investigated the contribution of load amplitude and sample geometry as major variables of fatigue failure via a statistical model to highlight the influnce of loading conditions. The obtianed results of our developed ML-based model in terms of paramertic analyses reveal that by inctreasing the surface modification factor (Fig. 11a), surface hardness (Fig. 11b), depth of CRS (Fig. 11c) and surface CRS (Fig. 11d), fatigue life is enhanced remarkably considering a fixed stress amplitude.

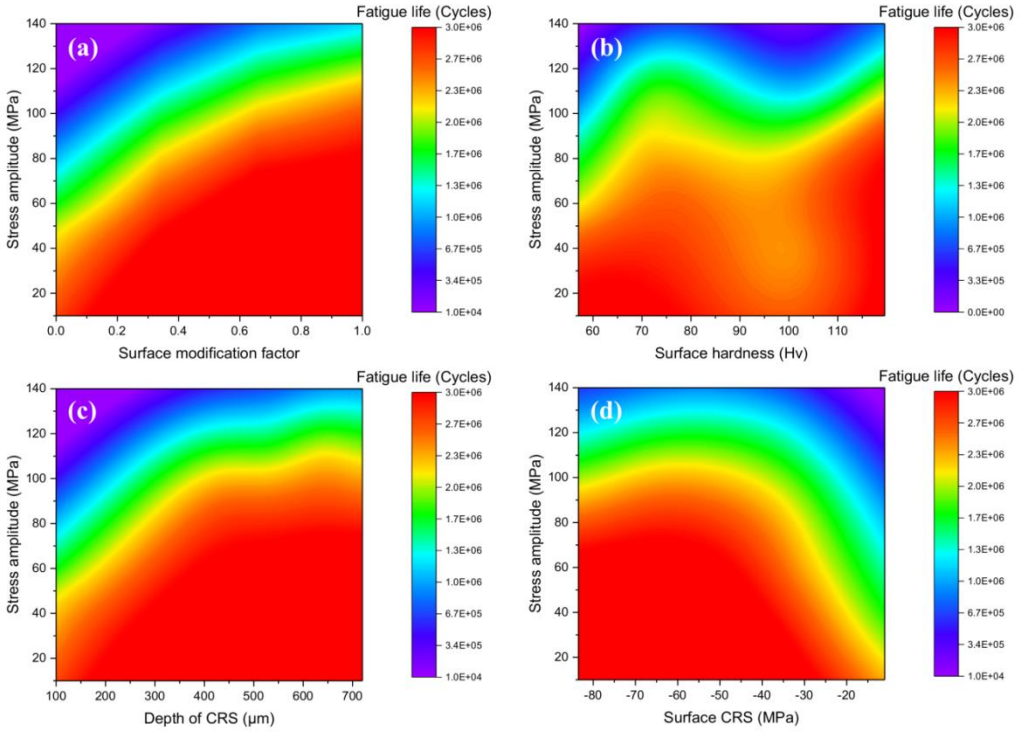

Fig. 11. Parametric analysis of the impact of inputs on fatigue life of notched LPBF AlSi10Mg samples in terms of (a) stress amplitude and surface modification factor, (b) stress amplitude and surface hardness, (c) stress amplitude and depth of CRS and (d) stress amplitude and surface CRS.

ML models offer the possibility of using a wide range of inputs, based on experimental tests for fatigue behavior prediction and analyses. In our study we have mostly focused on physical parameters that can be affected by post processing, including compressive residual stresses, surface roughness, microhardness, etc. Other possible ML-based approaches could include more details on microstructural features, local chemical composition, and plastic strains in the inputs of the modelling.

Furthermore, it should be mentioned that other types of ML-based models such as deep belief networks (DBNs) can be used for modelling additional aspects of the fatigue failure. DBNs have been widely used for instance for image classification and have a high potential to be used for evaluating fatigue behavior. These networks can be used for classification of the final quality of the AM fabricated parts in terms of porosity or surface morphology by implementing image processing. For example, it would be interesting to use these methods considering AM process parameters as inputs and pore density and pore shape as outputs of DBN models.

5. Conclusions

In the present study, an artificial neural network was used to assess the fatigue behavior of post-processed V-notched LPBF AlSi10Mg samples using a deep learning-based approach. The samples were considered in their as-built form and then post-processed utilizing a variety of various combinations of heat treatment and shot peening to get the desired results. The individual and combined impacts of various post-treatments on microstructure, surface state, microhardness, porosity, residual stresses, and fatigue behavior were investigated and employed to develop and evaluate the models. Deep neural networks with shallow, deep, and stacked auto-encoder assignments were constructed and evaluated in determining the most effective structure. The following findings may be obtained from the experiments and parametric and sensitivity analyses:

- The as-built samples exhibited an inhomogeneous microstructure as well as very low surface quality. Heat treatment homogenized the microstructure, whereas shot peening altered the surface morphology, increased the hardness of the surface layer, and caused substantial compressive residual stresses in the depth of the material.Fatigue life of the

notched samples was significantly improved by post-treatments especially after heat treatment followed by shot peening. However, considering the individual effect of each post-treatment, shot peening was found to be of higher efficiency for fatigue life improvement.

- The performance evaluation of developed shallow neural networks in terms of accuracy indicated that increasing the number of neurons in each layer, enhances the efficiency of the networks.
- By increasing the number of hidden layers the accuracy of the predicted results can be improved. For instance, developed shallow neural network with 2 hidden layers and deep neural network with 4 hidden layers revealed maximum accuracy of 95 and 97.5%, respectively.
- According to the modeling findings, the pre-trained stacked auto-encoder assigned deep neural networks demonstrated the best performance in terms of projected fatigue lifetimes, with an accuracy of more than 99% compared to the other deep neural networks.
- Considering parameters impacted by shot peening, the surface modification factor was shown to be the most beneficial parameter for improving fatigue life; homogeneity of the surface morphology was found to completely mask the deleterious effects of increased surface roughness following shot peening. In terms of fatigue life enhancement, increased surface hardness and compressive residual stresses on the surface, as well as the depth of compressive residual stresses, made significant contributions. Elongation was shown to be the most important of the characteristics affected by heat treatment when compared to yield and final strengths.
- By increasing the effect of shot peening on surface modification, surface hardness, surface compressive residual stresses and the depth of compressive residual stresses, fatigue life was remarkably improved considering a constant stress amplitude.
- Deep learning as a machine learning-based methodology was found to be an effective tool for predicting fatigue behavior and analyzing the influence of post-treatments on additively built materials when integrated with pre-training methods such as stacked auto-encoder.
- A refinement of the proposed model could distinguish the different fatigue failure mechanisms, leading to an even better understanding of the post-processing effects with respect of the fatigue failure mode.

Appendix A

Table A. Obtained experimental results arranged in terms of the considered input and output parameters used for developing the NNs

Set of sample	Sample No.	Yield stress (MPa)	Ultimate stress (MPa)	Elongation (%)	Relative density (%)	Surface hardness (Hv)	Depth of hardness variation (μm)	Surface CRS (MPa)	Maximum CRS (MPa)	Depth of CRS (μm)	Surface modification factor	Surface roughness, Ra (μm)	Stress amplitude (MPa)	Fatigue life (Cycle)
AB	1	273	393	2.5	99.53	101.4	0	-11	-57.6	100	0	4.34	60	376456
	2	273	393	2.5	99.53	101.4	0	-11	-57.6	100	0	4.34	30	1244634
	3	273	393	2.5	99.53	101.4	0	-11	-57.6	100	0	4.34	10	2203568
	4	273	393	2.5	99.53	101.4	0	-11	-57.6	100	0	4.34	20	1646240
	5	273	393	2.5	99.53	101.4	0	-11	-57.6	100	0	4.34	40	568620
	6	273	393	2.5	99.53	101.4	0	-11	-57.6	100	0	4.34	10	2362240
	7	273	393	2.5	99.53	101.4	0	-11	-57.6	100	0	4.34	110	13284
	8	273	393	2.5	99.53	101.4	0	-11	-57.6	100	0	4.34	110	10600
AB+SP1	9	273	393	2.5	99.48	109.7	190	-83.5	-157.7	530	0.5	4.52	110	1089200
	10	273	393	2.5	99.48	109.7	190	-83.5	-157.7	530	0.5	4.52	70	3000000
	11	273	393	2.5	99.48	109.7	190	-83.5	-157.7	530	0.5	4.52	90	2320000
	12	273	393	2.5	99.48	109.7	190	-83.5	-157.7	530	0.5	4.52	80	2110000
	13	273	393	2.5	99.48	109.7	190	-83.5	-157.7	530	0.5	4.52	70	2720000
	14	273	393	2.5	99.48	109.7	190	-83.5	-157.7	530	0.5	4.52	60	3000000
	15	273	393	2.5	99.48	109.7	190	-83.5	-157.7	530	0.5	4.52	80	3000000
	16	273	393	2.5	99.48	109.7	190	-83.5	-157.7	530	0.5	4.52	80	3000000
	17	273	393	2.5	99.48	109.7	190	-83.5	-157.7	530	0.5	4.52	90	2501100

	18	273	393	2.5	99.48	109.7	190	-83.5	-157.7	530	0.5	4.52	110	1200200
	19	273	393	2.5	99.48	109.7	190	-83.5	-157.7	530	0.5	4.52	110	1300010
	20	273	393	2.5	99.48	109.7	190	-83.5	-157.7	530	0.5	4.52	120	1020050
	21	273	393	2.5	99.48	109.7	190	-83.5	-157.7	530	0.5	4.52	120	921000
	22	273	393	2.5	99.48	109.7	190	-83.5	-157.7	530	0.5	4.52	130	753500
	23	273	393	2.5	99.48	109.7	190	-83.5	-157.7	530	0.5	4.52	130	687000
	24	273	393	2.5	99.48	109.7	190	-83.5	-157.7	530	0.5	4.52	140	401000
	25	273	393	2.5	99.48	109.7	190	-83.5	-157.7	530	0.5	4.52	140	500050
AB+SP2	26	273	393	2.5	99.56	119.6	240	-65.3	-164.3	440	1	4.83	60	3000000
	27	273	393	2.5	99.56	119.6	240	-65.3	-164.3	440	1	4.83	70	2835000
	28	273	393	2.5	99.56	119.6	240	-65.3	-164.3	440	1	4.83	70	3000000
	29	273	393	2.5	99.56	119.6	240	-65.3	-164.3	440	1	4.83	90	3000000
	30	273	393	2.5	99.56	119.6	240	-65.3	-164.3	440	1	4.83	110	2080000
	31	273	393	2.5	99.56	119.6	240	-65.3	-164.3	440	1	4.83	100	2599500
	32	273	393	2.5	99.56	119.6	240	-65.3	-164.3	440	1	4.83	90	2844026
	33	273	393	2.5	99.56	119.6	240	-65.3	-164.3	440	1	4.83	80	3000000
	34	273	393	2.5	99.56	119.6	240	-65.3	-164.3	440	1	4.83	80	3000000
	35	273	393	2.5	99.56	119.6	240	-65.3	-164.3	440	1	4.83	90	3000000
	36	273	393	2.5	99.56	119.6	240	-65.3	-164.3	440	1	4.83	100	3000000
	37	273	393	2.5	99.56	119.6	240	-65.3	-164.3	440	1	4.83	110	1989000
	38	273	393	2.5	99.56	119.6	240	-65.3	-164.3	440	1	4.83	110	2290000
	39	273	393	2.5	99.56	119.6	240	-65.3	-164.3	440	1	4.83	120	1704087
	40	273	393	2.5	99.56	119.6	240	-65.3	-164.3	440	1	4.83	120	1560000
	41	273	393	2.5	99.56	119.6	240	-65.3	-164.3	440	1	4.83	130	1032000
	42	273	393	2.5	99.56	119.6	240	-65.3	-164.3	440	1	4.83	130	1400040
	43	273	393	2.5	99.56	119.6	240	-65.3	-164.3	440	1	4.83	140	723000
AB+HT	44	201	265	13	99.61	57	0	-30.3	-44	100	0	4.3	40	3000000
	45	201	265	13	99.61	57	0	-30.3	-44	100	0	4.3	50	2398000
	46	201	265	13	99.61	57	0	-30.3	-44	100	0	4.3	30	3000000
	47	201	265	13	99.61	57	0	-30.3	-44	100	0	4.3	50	3000000
	48	201	265	13	99.61	57	0	-30.3	-44	100	0	4.3	60	1459000
	49	201	265	13	99.61	57	0	-30.3	-44	100	0	4.3	50	2607900
	50	201	265	13	99.61	57	0	-30.3	-44	100	0	4.3	40	2820000
	51	201	265	13	99.61	57	0	-30.3	-44	100	0	4.3	50	2558297
	52	201	265	13	99.61	57	0	-30.3	-44	100	0	4.3	60	1301000
	53	201	265	13	99.61	57	0	-30.3	-44	100	0	4.3	40	2510000
	54	201	265	13	99.61	57	0	-30.3	-44	100	0	4.3	30	3000000
	55	201	265	13	99.61	57	0	-30.3	-44	100	0	4.3	40	2700000
	56	201	265	13	99.61	57	0	-30.3	-44	100	0	4.3	110	25200
	57	201	265	13	99.61	57	0	-30.3	-44	100	0	4.3	110	22100
AB+HT+SP1	58	201	265	13	99.58	76.3	190	-46.6	-113.6	720	0.5	4.56	110	1820000
	59	201	265	13	99.58	76.3	190	-46.6	-113.6	720	0.5	4.56	90	2368650
	60	201	265	13	99.58	76.3	190	-46.6	-113.6	720	0.5	4.56	70	3000000
	61	201	265	13	99.58	76.3	190	-46.6	-113.6	720	0.5	4.56	90	2675210
	62	201	265	13	99.58	76.3	190	-46.6	-113.6	720	0.5	4.56	80	3000000
	63	201	265	13	99.58	76.3	190	-46.6	-113.6	720	0.5	4.56	80	3000000
	64	201	265	13	99.58	76.3	190	-46.6	-113.6	720	0.5	4.56	100	1921150
	65	201	265	13	99.58	76.3	190	-46.6	-113.6	720	0.5	4.56	90	2318480
	66	201	265	13	99.58	76.3	190	-46.6	-113.6	720	0.5	4.56	80	2585590
	67	201	265	13	99.58	76.3	190	-46.6	-113.6	720	0.5	4.56	110	1978500
	68	201	265	13	99.58	76.3	190	-46.6	-113.6	720	0.5	4.56	110	2142000
	69	201	265	13	99.58	76.3	190	-46.6	-113.6	720	0.5	4.56	120	1340000
	70	201	265	13	99.58	76.3	190	-46.6	-113.6	720	0.5	4.56	130	1300500
	71	201	265	13	99.58	76.3	190	-46.6	-113.6	720	0.5	4.56	140	743200
	72	201	265	13	99.58	76.3	190	-46.6	-113.6	720	0.5	4.56	120	1620000
	73	201	265	13	99.58	76.3	190	-46.6	-113.6	720	0.5	4.56	130	1010200
	74	201	265	13	99.58	76.3	190	-46.6	-113.6	720	0.5	4.56	140	801000
AB+HT+SP2	75	201	265	13	99.57	72	190	-31.7	-103.8	640	1	4.87	110	2620000
	76	201	265	13	99.57	72	190	-31.7	-103.8	640	1	4.87	90	2525170
	77	201	265	13	99.57	72	190	-31.7	-103.8	640	1	4.87	80	3000000
	78	201	265	13	99.57	72	190	-31.7	-103.8	640	1	4.87	100	3000000
	79	201	265	13	99.57	72	190	-31.7	-103.8	640	1	4.87	120	3000000
	80	201	265	13	99.57	72	190	-31.7	-103.8	640	1	4.87	140	1000800

81	201	265	13	99.57	72	190	-31.7	-103.8	640	1	4.87	120	2261770
82	201	265	13	99.57	72	190	-31.7	-103.8	640	1	4.87	100	2393060
83	201	265	13	99.57	72	190	-31.7	-103.8	640	1	4.87	80	3000000
84	201	265	13	99.57	72	190	-31.7	-103.8	640	1	4.87	90	3000000
85	201	265	13	99.57	72	190	-31.7	-103.8	640	1	4.87	110	3000000
86	201	265	13	99.57	72	190	-31.7	-103.8	640	1	4.87	110	3000000
87	201	265	13	99.57	72	190	-31.7	-103.8	640	1	4.87	140	906500
88	201	265	13	99.57	72	190	-31.7	-103.8	640	1	4.87	130	1430700
89	201	265	13	99.57	72	190	-31.7	-103.8	640	1	4.87	130	1750120

Appendix B

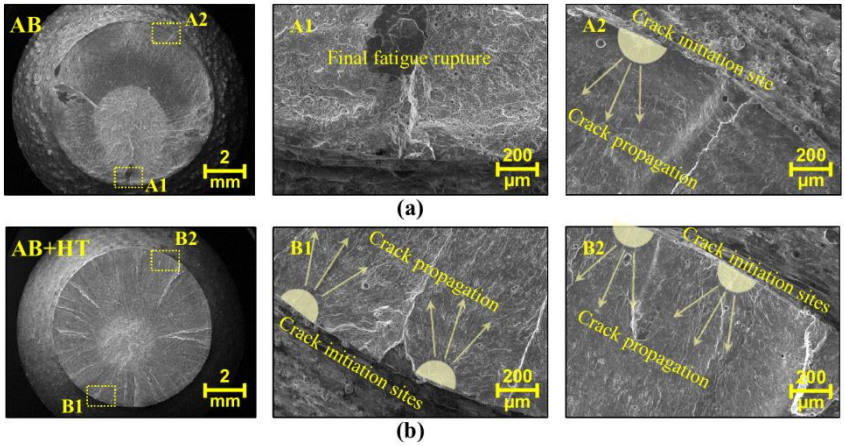

Fig. B. SEM images of fracture surfaces of (a) AB and (b) AB+HT samples focusing on crack initiation sites.

Appendix C

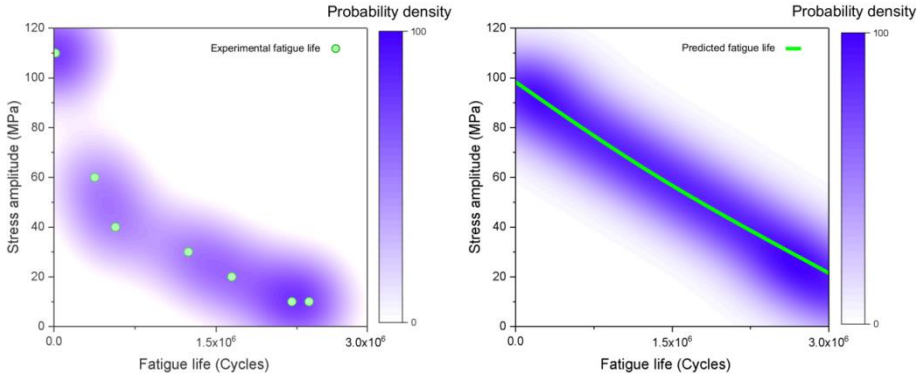

Fig. C. Probability density analyses of the experimental and predicted results for AB sample.

Conflict of interest

The authors declare they have no conflict of interests.

References

[1] Gardan J. Additive manufacturing technologies: State of the art and trends. Int J Prod Res 2016. https://doi.org/10.1080/00207543.2015.1115909.

[2] DebRoy T, Wei HL, Zuback JS, Mukherjee T, Elmer JW, Milewski JO, et al. Additive manufacturing of metallic components – Process, structure and properties. Prog Mater Sci 2018. https://doi.org/10.1016/j.pmatsci.2017.10.001.

[3] Gokcekaya O, Hayashi N, Ishimoto T, Ueda K, Narushima T, Nakano T. Crystallographic orientation control of pure chromium via laser powder bed fusion and improved high temperature oxidation resistance. Addit Manuf 2020. https://doi.org/10.1016/j.addma.2020.101624.

[4] Liu X, Zhao C, Zhou X, Shen Z, Liu W. Microstructure of selective laser melted AlSi10Mg alloy. Mater Des 2019. https://doi.org/10.1016/j.matdes.2019.107677.

[5] Tang M, Pistorius PC, Narra S, Beuth JL. Rapid Solidification: Selective Laser Melting of AlSi10Mg. JOM 2016. https://doi.org/10.1007/s11837-015-1763-3.
[6] Yadroitsev I, Smurov I. Surface morphology in selective laser melting of metal powders. Phys. Procedia, 2011. https://doi.org/10.1016/j.phpro.2011.03.034.
[7] Herzog D, Seyda V, Wycisk E, Emmelmann C. Additive manufacturing of metals. Acta Mater 2016. https://doi.org/10.1016/j.actamat.2016.07.019.
[8] Ferro P, Fabrizi A, Berto F, Savio G, Meneghello R, Rosso S. Defects as a root cause of fatigue weakening of additively manufactured AlSi10Mg components. Theor Appl Fract Mech 2020. https://doi.org/10.1016/j.tafmec.2020.102611.
[9] Aboulkhair NT, Everitt NM, Ashcroft I, Tuck C. Reducing porosity in AlSi10Mg parts processed by selective laser melting. Addit Manuf 2014. https://doi.org/10.1016/j.addma.2014.08.001.
[10] Mfusi BJ, Mathe NR, Tshabalala LC, Popoola PAI. The effect of stress relief on the mechanical and fatigue properties of additively manufactured AlSi10Mg parts. Metals (Basel) 2019. https://doi.org/10.3390/met9111216.
[11] Mukherjee T, Zhang W, DebRoy T. An improved prediction of residual stresses and distortion in additive manufacturing. Comput Mater Sci 2017. https://doi.org/10.1016/j.commatsci.2016.10.003.
[12] Hamidi Nasab M, Gastaldi D, Lecis NF, Vedani M. On morphological surface features of the parts printed by selective laser melting (SLM). Addit Manuf 2018. https://doi.org/10.1016/j.addma.2018.10.011.
[13] Xu Z, Liu A, Wang X. Fatigue performance and crack propagation behavior of selective laser melted AlSi10Mg in 0°, 15°, 45° and 90° building directions. Mater Sci Eng A 2021. https://doi.org/10.1016/j.msea.2021.141141.
[14] Beretta S, Gargourimotlagh M, Foletti S, du Plessis A, Riccio M. Fatigue strength assessment of “as built” AlSi10Mg manufactured by SLM with different build orientations. Int J Fatigue 2020. https://doi.org/10.1016/j.ijfatigue.2020.105737.
[15] Maleki E, Bagherifard S, Sabouri F, Bandini M, Guagliano M. Hybrid thermal, mechanical and chemical surface post-treatments for improved fatigue behavior of laser powder bed fusion AlSi10Mg samples with notched geometry. Surf Coat Technol 2021. https://doi.org/10.1016/j.surfcoat.2021.127962.
[16] Sames WJ, List FA, Pannala S, Dehoff RR, Babu SS. The metallurgy and processing science of metal additive manufacturing. Int Mater Rev 2016. https://doi.org/10.1080/09506608.2015.1116649.
[17] Zhang Z, Sun C, Xu X, Liu L. Surface quality and forming characteristics of thin-wall aluminium alloy parts manufactured by laser assisted MIG arc additive manufacturing. Int J Light Mater Manuf 2018. https://doi.org/10.1016/j.ijlmm.2018.03.005.
[18] Li R, Liu J, Shi Y, Wang L, Jiang W. Balling behavior of stainless steel and nickel powder during selective laser melting process. Int J Adv Manuf Technol 2012. https://doi.org/10.1007/s00170-011-3566-1.
[19] Maleki E, Bagherifard S, Bandini M, Guagliano M. Surface post-treatments for metal additive manufacturing: Progress, challenges, and opportunities. Addit Manuf 2021;37:101619. https://doi.org/10.1016/j.addma.2020.101619.
[20] Uzan NE, Ramati S, Shneck R, Frage N, Yeheskel O. On the effect of shot-peening on fatigue resistance of AlSi10Mg specimens fabricated by additive manufacturing using selective laser melting (AM-SLM). Addit Manuf 2018. https://doi.org/10.1016/j.addma.2018.03.030.
[21] Leon A, Aghion E. Effect of surface roughness on corrosion fatigue performance of AlSi10Mg alloy produced by Selective Laser Melting (SLM). Mater Charact 2017. https://doi.org/10.1016/j.matchar.2017.06.029.
[22] Lewandowski JJ, Seifi M. Metal Additive Manufacturing: A Review of Mechanical Properties. Annu Rev Mater Res 2016. https://doi.org/10.1146/annurev-matsci-070115-032024.
[23] Balachandramurthi AR, Moverare J, Dixit N, Pederson R. Influence of defects and as-built surface roughness on fatigue properties of additively manufactured Alloy 718. Mater Sci Eng A 2018. https://doi.org/10.1016/j.msea.2018.08.072.
[24] Maleki E, Unal O, Guagliano M, Bagherifard S. The effects of shot peening, laser shock

peening and ultrasonic nanocrystal surface modification on the fatigue strength of Inconel 718. Mater Sci Eng A 2021;810. https://doi.org/10.1016/j.msea.2021.141029.
[25] Maleki N, Kashanian S, Maleki E, Nazari M. A novel enzyme based biosensor for catechol detection in water samples using artificial neural network. Biochem Eng J 2017;128:1–11. https://doi.org/10.1016/j.bej.2017.09.005.
[26] Maleki E, Unal O. Shot Peening Process Effects on Metallurgical and Mechanical Properties of 316 L Steel via: Experimental and Neural Network Modeling. Met Mater Int 2019. https://doi.org/10.1007/s12540-019-00448-3.
[27] Maleki E, Unal O. Optimization of Shot Peening Effective Parameters on Surface Hardness Improvement. Met Mater Int 2020. https://doi.org/10.1007/s12540-020-00758-x.
[28] Maleki N, Maleki E. Modeling of cathode Pt /C electrocatalyst degradation and performance of a PEMFC using artificial neural network. ACM Int. Conf. Proceeding Ser., vol. 24-26- Sept, 2015. https://doi.org/10.1145/2832987.2833000.
[29] Maleki E, Unal O, Reza Kashyzadeh K. Fatigue behavior prediction and analysis of shot peened mild carbon steels. Int J Fatigue 2018;116:48–67. https://doi.org/10.1016/j.ijfatigue.2018.06.004.
[30] Livingstone DJ, Manallack DT, Tetko I V. Data modelling with neural networks: Advantages and limitations. J Comput Aided Mol Des 1997. https://doi.org/10.1023/A:1008074223811.
[31] Hinton GE, Osindero S, Teh YW. A fast learning algorithm for deep belief nets. Neural Comput 2006. https://doi.org/10.1162/neco.2006.18.7.1527.
[32] Hinton GE, Salakhutdinov RR. Reducing the dimensionality of data with neural networks. Science (80-) 2006. https://doi.org/10.1126/science.1127647.
[33] Bengio Y, Lamblin P, Popovici D, Larochelle H. Greedy layer-wise training of deep networks. Adv. Neural Inf. Process. Syst., 2007. https://doi.org/10.7551/mitpress/7503.003.0024.
[34] Feng S, Zhou H, Dong H. Using deep neural network with small dataset to predict material defects. Mater Des 2019;162:300–10. https://doi.org/10.1016/j.matdes.2018.11.060.
[35] Liu G, Bao H, Han B. A Stacked Autoencoder-Based Deep Neural Network for Achieving Gearbox Fault Diagnosis. Math Probl Eng 2018. https://doi.org/10.1155/2018/5105709.
[36] Wang Y Bin, You ZH, Li X, Jiang TH, Chen X, Zhou X, et al. Predicting protein-protein interactions from protein sequences by a stacked sparse autoencoder deep neural network. Mol Biosyst 2017. https://doi.org/10.1039/c7mb00188f.
[37] Qi X, Chen G, Li Y, Cheng X, Li C. Applying Neural-Network-Based Machine Learning to Additive Manufacturing: Current Applications, Challenges, and Future Perspectives. Engineering 2019;5:721–9. https://doi.org/10.1016/j.eng.2019.04.012.
[38] Garg A, Tai K, Savalani MM. Formulation of bead width model of an SLM prototype using modified multi-gene genetic programming approach. Int J Adv Manuf Technol 2014;73:375–88. https://doi.org/10.1007/s00170-014-5820-9.
[39] Saqiba S, Urbanica RJ, Aggarwal K. Analysis of laser cladding bead morphology for developing additive manufacturing travel paths. Procedia CIRP 2014;17:824–9. https://doi.org/10.1016/j.procir.2014.01.098.
[40] Marrey M, Malekipour E, El-Mounayri H, Faierson EJ. A framework for optimizing process parameters in powder bed fusion (PBF) process using artificial neural network (ANN). Procedia Manuf 2019;34:505–15. https://doi.org/10.1016/j.promfg.2019.06.214.
[41] Xiong J, Zhang G, Hu J, Wu L. Bead geometry prediction for robotic GMAW-based rapid manufacturing through a neural network and a second-order regression analysis. J Intell Manuf 2014. https://doi.org/10.1007/s10845-012-0682-1.
[42] Zhang B, Liu S, Shin YC. In-Process monitoring of porosity during laser additive manufacturing process. Addit Manuf 2019. https://doi.org/10.1016/j.addma.2019.05.030.
[43] Zhan Z, Li H. Machine learning based fatigue life prediction with effects of additive manufacturing process parameters for printed SS 316L. Int J Fatigue 2021. https://doi.org/10.1016/j.ijfatigue.2020.105941.
[44] Zhan Z, Li H. A novel approach based on the elastoplastic fatigue damage and machine learning models for life prediction of aerospace alloy parts fabricated by additive manufacturing. Int J Fatigue 2021. https://doi.org/10.1016/j.ijfatigue.2020.106089.
[45] Mozaffar M, Paul A, Al-Bahrani R, Wolff S, Choudhary A, Agrawal A, et al. Data-driven

prediction of the high-dimensional thermal history in directed energy deposition processes via recurrent neural networks. Manuf Lett 2018;18:35–9. https://doi.org/10.1016/j.mfglet.2018.10.002.
[46] Scime L, Beuth J. A multi-scale convolutional neural network for autonomous anomaly detection and classification in a laser powder bed fusion additive manufacturing process. Addit Manuf 2018;24:273–86. https://doi.org/10.1016/j.addma.2018.09.034.
[47] Kwon O, Kim HG, Ham MJ, Kim W, Kim GH, Cho JH, et al. A deep neural network for classification of melt-pool images in metal additive manufacturing. J Intell Manuf 2018;31:375–86. https://doi.org/10.1007/s10845-018-1451-6.
[48] Maleki E, Bagherifard S, Guagliano M. Application of artificial intelligence to optimize the process parameters effects on tensile properties of Ti-6Al-4V fabricated by laser powder-bed fusion. Int J Mech Mater Des 2021. https://doi.org/10.1007/s10999-021-09570-w.
[49] Maleki E, Bagherifard S, Razavi SMJSMJ, Riccio M, Bandini M, du Plessis A, et al. Fatigue behaviour of notched laser powder bed fusion AlSi10Mg after thermal and mechanical surface post-processing. Mater Sci Eng A 2022;829:142145. https://doi.org/10.1016/j.msea.2021.142145.
[50] Maleki E, Farrahi GH, Reza Kashyzadeh K, Unal O, Gugaliano M, Bagherifard S. Effects of Conventional and Severe Shot Peening on Residual Stress and Fatigue Strength of Steel AISI 1060 and Residual Stress Relaxation Due to Fatigue Loading: Experimental and Numerical Simulation. Met Mater Int 2020. https://doi.org/10.1007/s12540-020-00890-8.
[51] EN ISO 4287. Geometrical Product Specifications (GPS) - Surface texture: Profile method - Terms, definitions and surface texture parameters. Int Organ Stand 1997.
[52] Maleki E, Unal O. Fatigue limit prediction and analysis of nano-structured AISI 304 steel by severe shot peening via ANN. Eng Comput 2020. https://doi.org/10.1007/s00366-020-00964-6.
[53] Maleki E, Unal O, Guagliano M, Bagherifard S. Analysing the Fatigue Behaviour and Residual Stress Relaxation of Gradient Nano-structured 316L Steel Subjected to the Shot Peening via Deep Learning Approach. Met Mater Int 2021. https://doi.org/10.1007/s12540-021-00995-8.
[54] Maleki E. Artificial neural networks application for modeling of friction stir welding effects on mechanical properties of 7075-T6 aluminum alloy. IOP Conf. Ser. Mater. Sci. Eng., vol. 103, 2015. https://doi.org/10.1088/1757-899X/103/1/012034.
[55] Bagherifard S, Beretta N, Monti S, Riccio M, Bandini M, Guagliano M. On the fatigue strength enhancement of additive manufactured AlSi10Mg parts by mechanical and thermal post-processing. Mater Des 2018;145:28–41. https://doi.org/10.1016/j.matdes.2018.02.055.
[56] Yamanaka A, Kamijyo R, Koenuma K, Watanabe I, Kuwabara T. Deep neural network approach to estimate biaxial stress-strain curves of sheet metals. Mater Des 2020. https://doi.org/10.1016/j.matdes.2020.108970.
[57] Olden JD, Joy MK, Death RG. An accurate comparison of methods for quantifying variable importance in artificial neural networks using simulated data. Ecol Modell 2004. https://doi.org/10.1016/j.ecolmodel.2004.03.013.
[58] Razavi SMJ, Van Hooreweder B, Berto F. Effect of build thickness and geometry on quasi-static and fatigue behavior of Ti-6Al-4V produced by Electron Beam Melting. Addit Manuf 2020. https://doi.org/10.1016/j.addma.2020.101426.
[59] Maleki E, Mirzaali MJ, Guagliano M, Bagherifard S. Analyzing the mechano-bactericidal effect of nano-patterned surfaces on different bacteria species. Surf Coatings Technol 2020. https://doi.org/10.1016/j.surfcoat.2020.126782.
[60] Girelli L, Giovagnoli M, Tocci M, Pola A, Fortini A, Merlin M, et al. Evaluation of the impact behaviour of AlSi10Mg alloy produced using laser additive manufacturing. Mater Sci Eng A 2019. https://doi.org/10.1016/j.msea.2019.01.078.
[61] Qian G, Li Y, Paolino DS, Tridello A, Berto F, Hong Y. Very-high-cycle fatigue behavior of Ti-6Al-4V manufactured by selective laser melting: Effect of build orientation. Int J Fatigue 2020. https://doi.org/10.1016/j.ijfatigue.2020.105628.
[62] Maleki E, Unal O, Reza Kashyzadeh K. Surface layer nanocrystallization of carbon steels subjected to severe shot peening: Analysis and optimization. Mater Charact 2019;157:109877.

https://doi.org/10.1016/j.matchar.2019.109877.
[63] Qian G, Lei WS. A statistical model of fatigue failure incorporating effects of specimen size and load amplitude on fatigue life. Philos Mag 2019. https://doi.org/10.1080/14786435.2019.1609707.